Polymer Testing 128 (2023) 108238

Contents lists available at ScienceDirect

Polymer Testing

journal homepage: www.elsevier.com/locate/polytest

Characterization of the physical properties of the thermoresponsive block-copolymer PAGB2000 and numerical assessment of its potentialities in Forward Osmosis desalination

Igor Matteo Carraretto [a,*], Vincenzo Ruzzi [b], Filippo Lodigiani [a], Rosemary Colciaghi [a], Riccardo Simonetti [a], Stefano Buzzaccaro [b], Luca Molinaroli [a], Luigi Pietro Maria Colombo [a], Roberto Piazza [b], Giampaolo Manzolini [a]

[a] Dipartimento di Energia, Politecnico di Milano, Via Lambruschini 4, Milano 20156, Italy
[b] Dipartimento di Chimica, Materiali e Ingegneria Chimica "Giulio Natta", Politecnico di Milano, P.zza Leonardo da Vinci 32, Milano 20133, Italy

ARTICLE INFO

Keywords:
Polymer
Draw agent
Forward osmosis
Desalination

ABSTRACT

Forward Osmosis is a promising strategy for desalination processes, however some aspects have to be better characterized to make it competitive with other affirmed technologies. One of these aspects is the selection of the draw agent, i.e., a polymeric solution that has to fulfill different requirements to guarantee both high membrane performances and good regeneration process. Previous studies have identified a thermoresponsive copolymer known as PAGB2000 as potential draw agent. However, in the open literature there is no information on the thermo-physical properties required for a fully characterization of the polymer itself, hence, different experimental campaigns have been conducted to quantify: phase behavior, osmotic pressure, density, dynamic viscosity, thermal conductivity, thermal diffusivity and isobaric specific heat capacity. These properties were then used in a computational model to simulate the whole desalination process. Recovery ratio, specific electric consumption and specific thermal consumption were compared with the ones obtained in a previous work, showing that a detailed characterization of the thermo-physical properties is required to get accurate and realistic predictions of the system performance.

1. Introduction

Water is fundamental for humankind, however, at present, one-fifth of the global population is dealing with water scarcity [1]. Additionally, one-fourth of the population lacks suitable means for water purification in spite of having access to water sources [1]. This crisis is expected to worsen. According to the United Nations World Assessment Program (UNESCO, Paris 2015) about 40% of the population will experience water scarcity by 2030 [1]. This is mainly linked to the fact that only the 3% of the overall water reserves is available as freshwater (i.e., glaciers, ice caps), with seawater representing the remaining percentage [2]. Climate change and population growth are additional factors that threaten the future availability of freshwater [2]. Even if the improvement and conservation of the existing water facilities are crucial, additional freshwater accessibility must be guaranteed to tackle the compelling water crisis [2].

In this prospective it is clear that desalination might play a primary role considering the large quantity of saline water on the Earth. In general terms, desalination is the purification process used to obtain fresh or potable water from available saline water (i.e., seawater, brackish water [1], and brine [3]). Desalination systems can be divided into two groups according to the technology adopted: membrane-based and thermal-based. The Membrane-based technologies typically exploit mechanical pressure, electrical energy (electrical potential difference) or concentration variations as driving factor to cross a semipermeable membrane, resulting in physical separation. To cite some: Electrodialysis (ED) [4], Reverse Osmosis (RO) [4], Forward Osmosis (FO) [4] and Membrane Distillation (MD) [4]. On the other hand, the thermal methods rely on phase change process and include Multi-Stage Flash Distillation (MSF) [4], Multi-Effect Distillation (MED) [4], Humidification–Dehumidification (HDH) [5], and Vapor Compression Distillation (VCD) [4].

Among the one reported, RO is the most mature technology accounting for 84% of the total number of operating desalination plants, and contributing with a share of 65% to the desalinated water globally produced [2]. However, in the last decades the membrane-based

* Corresponding author.
E-mail addresses: igormatteo.carraretto@polimi.it (I.M. Carraretto), vincenzo.ruzzi@polimi.it (V. Ruzzi).

https://doi.org/10.1016/j.polymertesting.2023.108238
Received 12 May 2023; Received in revised form 23 September 2023; Accepted 5 October 2023
Available online 8 October 2023

Nomenclature

c	Mass concentration (kg/kg)
c_p	Isobaric specific heat capacity (J/kg K)
k	Thermal conductivity (W/m K)
n	Refractive index (–)
p	Pressure (bar)
T	Temperature (°C)
T_0	Reference Temperature (K)

Greek

α	Thermal diffusivity (mm^2/s)
μ	Dynamic viscosity (cP)
π	Osmotic pressure (bar)
ρ	Density (kg/m^3)

Subscripts

meas	Experimentally determined value
mod	Modeled value

technology of FO is getting attention by both researchers and industry, representing a possible alternative to high electric-consuming RO process.

The driving force of FO processes is the difference in the osmotic pressure that establishes between the feed solution to treat (i.e., seawater), showing the lower osmotic pressure, and the more concentrated draw solution (DS). In reason of this pressure difference, water diffuses across the membrane, from the less concentrated side, diluting the draw solute and balancing the concentration levels; whereas the solute or salt molecules in the feed solution are rejected [6]. The obtained diluted DS has to be further treated to separate the water (now freshwater) from the DS (now re-concentrated), making the latter reusable for a new dilution. The aspect of not relying on the application of external hydraulic pressure along with the fact that both low membrane fouling and a greater water recovery are expected [7], justify the increasing interest for this new desalination technology. Up to now, researchers are mainly focused on studying two crucial aspects: membranes and draw solutes.

Focusing on the draw solutions available, as reported by Long et al. in [8], they can be classified on the type of energy required to perform the regeneration and six categories are identified: (1) direct use, (2) chemical energy, (3) waste heat/thermal energy, (4) electric energy, (5) solar energy/irradiating, and (6) magnetic field energy. Among these types, the most interesting for this work, and for low-grade heat applications in general, is represented by the thermally regenerative DSs, being a more cost-effective solution compared to the others [8]. Currently, different kinds of DS, that are regenerated providing heat power, are reported in the open literature, to cite few: (1) gas and volatile compounds [9], (2) phase transition materials (such as lower/upper critical solution temperature (LCST [10]/UCST [11]) compounds and thermo-sensitive gels [12]), and (3) membrane distillations [13]. In particular, phase transition materials exhibit unique phase behavior, characterized by a temperature-dependent miscibility with water. In Lower Critical Solution Temperature (LCST) mixtures the two liquid components are miscible below a certain temperature level, *vice versa* in upper critical solution temperature (UCST) mixtures the miscibility is achieved above a certain temperature level.

In a previous work by Colciaghi et al. [14], which stands on the works of Inada et al. [15,16], both an Ammonium Based (AB) and three different poly (propylene glycol-ran-ethylene glycol) monobutyl ethers (PAGBs), namely PAGB1000, PAGB2000 and PAGB4000, have been considered as draw agents. From the analysis conducted resulted that PAGB1000 and PAGB2000 have very similar consumption trends.

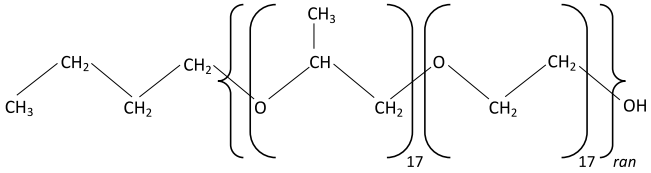

Fig. 1. Structural formula of the PAGB2000 copolymer.

PAGB1000 has lower electrical consumptions and higher water flux, but it is penalized in the regeneration step, as it has the higher regeneration temperature (T_{reg}) among the selected polymers (i.e., 77.2 °C for PAGB2000, 83.6 °C for PAGB1000 and 80.1 °C for PAGB4000,). Hence, PAGB2000 shows overall better performances compared with the other two polymers, and it was selected as draw agent.

However, from the literature analysis conducted, very few and sparse information can be found on PAGB2000 thermo-physical properties, which on the other hand are fundamental to understand both the feasibility and the function of a desalination power plant with FO technology. Hence, an extensive experimental campaign is conducted to fully characterize this polymer, to be efficiently used as draw agent in FO desalination power plant.

2. Materials and methods

2.1. Materials and sample preparation

The selected thermoresponsive draw agent is a poly (propylene glycol-ran-ethylene glycol) monobutyl ether with molar mass of $M_w \simeq 1810$ Da (PAGB2000). This block copolymer has a chemical structure C_4H_9–$[(C_2H_40)_{17}$–$(C_3H_60)_{17}]_{ran}$–OH (see Fig. 1 for the structural formula), with a butyl ether group bonded to the amphiphilic part composed by an equal number of random copolymerized propylenoxyde and ethylenoxyde groups. It appears as a highly viscous and colorless liquid that is miscible with water at any ratio.

In our study, PAGB2000, known with the commercial name of UNILUBE 50MB-26, is purchased from NOF Corporation® (Tokyo, Japan) and used without further purification. The aqueous samples employed for the characterization are prepared on an analytic scale (sensitivity 10^{-4} g) by slowly dissolving the polymer in distilled water. After the dissolution, the samples are gently mixed by hand in order to ensure a perfect homogenization and kept in a refrigerator waiting for the complete removal of air bubbles that unavoidably show up while shaking the polymer solution.

2.2. Methods

In this section, we provide a description of the methods used to measure the physical properties of the PAGB2000 aqueous solutions. Unless otherwise stated, all quantities are determined in the temperature range 20–40 °C and in the whole concentration interval, ranging from distilled water to pure polymer.

2.2.1. Refractive index

The refractive index n of the polymer solutions is evaluated in order to determine the polymer content in the phase-separated samples and as auxiliary data for the optical methods. The refractive index is measured with a temperature-controlled Abbemat RXA digital refractometer (Anton Paar, Graz, Austria), with a sensitivity $\Delta n \simeq 10^{-5}$.

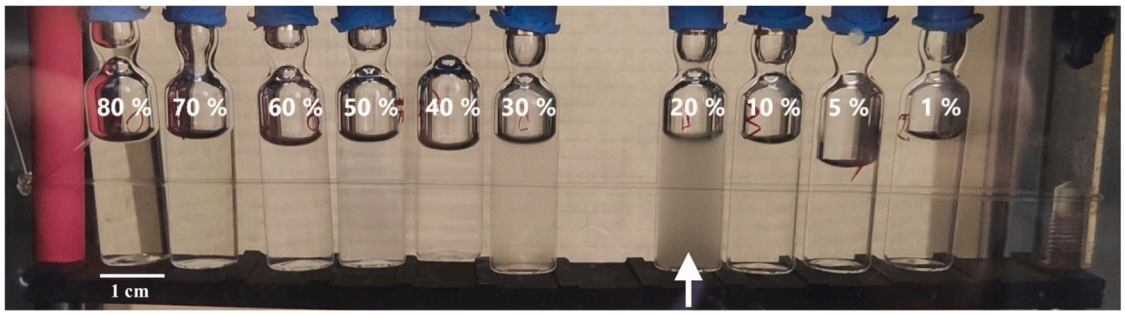

Fig. 2. Picture of the preliminary phase separation experiment taken at $T \simeq 40$ °C. Each sample is labeled with its nominal weight percent concentration. The white arrow points to the most turbid sample that is phase-separating at $c = 0.2$.

2.2.2. Phase diagram

The phase separation points of the PAGB2000 solution are determined inserting the polymer solutions in a water thermostat (Haake F3, Thermo Fisher Scientific, Waltham (MA), United States, 0.1 °C sensitivity) with a window allowing for optical inspection. As a preliminary analysis, ten samples at different concentrations ranging from 0.01 to 0.8, are sealed in glass ampules and submerged in the thermal bath; the temperature is gradually raised from $T = 20$ °C until we observed the sample at $c = 0.2$ becoming turbid at $T \simeq 40$ °C, marking therefore the incipient phase separation, as shown in Fig. 2. Then, nine different samples at $c = 0.2$ are immersed in the water thermostat at $T = 20$ °C and the phase separation is studied for each sample at a different temperature level from 43 °C to 80 °C. Once each temperature level is reached, the system thermalizes for at least half an hour in order to complete the separation in the polymer-rich and polymer-poor phases. When the transition is over, the diluted and concentrated phases are collected and stored separately at room temperature. The refractive indexes of the two phase-separated samples are then measured at $T = 20$ °C and their concentration is retrieved from the calibration curve obtained at the same temperature (see Fig. 3(b)).

2.2.3. Osmotic pressure

The osmotic pressure of the polymer solution is evaluated with Static Light Scattering (SLS), an optical technique in which the laser light scattered by a fluid sample is collected at a given angle by a quadratic detector, allowing us to assess microscopic structural information of the sample at a lenghtscale comparable to the probing wavelength.

In general, a macro-molecular fluid can be described as a continuum in which the presence of molecules causes refractive index fluctuations which, in turns, are responsible for the elastic spreading of the incident radiation. These variations are related to concentration fluctuations, from which the osmotic compressibility and then the *osmotic pressure* can be retrieved. Consider an incident laser beam with wavelength λ and a detector placed at an angle θ which reveals the scattered intensity from a sample with refractive index n. Assuming an isotropic medium with point-like scatterers (the molecules in solution), thus working in the so-called Rayleigh regime, it can be shown [17] that the scattered intensity $I_s(q)$ at a given wave vector $q = 4\pi n(\sin\theta/2)/\lambda$ is proportional to the averaged-squared refractive index fluctuations $\langle \delta n(q)^2 \rangle$ $\left(I_s(q) \propto \langle |\delta n(q)|^2 \rangle\right)$. Fluctuations can be associated to local variations of polymer concentration $c(\mathbf{r})$, therefore we can write:

$$n(\mathbf{r}) \equiv n[c(\mathbf{r})] \simeq n(\bar{c}) + (\partial n/\partial c)\delta c(\mathbf{r}), \tag{1}$$

where $\bar{c}$ is the macroscopic concentration and $n(\bar{c}) = n$. Thus, we obtain:

$$I_s(q) \propto \left(\frac{\partial n}{\partial c}\right)^2 \langle |\delta c(q)|^2 \rangle. \tag{2}$$

As, in our case, the wavelength is always much larger than the average distance between the scatterers, we always look at the laser intensity I_s scattered at $q = 0$, whatever is the detection angle. The concentration fluctuations at $q = 0$ (thus associated to the whole sample) are related to osmotic compressibility $\chi_c = (1/c)(\partial\pi/\partial c)^{-1}$ by the fluctuation–dissipation theorem, a general result relating spontaneous fluctuations of a given quantity to the response functions of a system [18]. Quantitatively, we can write: $\langle |\delta c(0)|^2 \rangle = (k_B T c^2/V)\chi_c$, where k_B is the Boltzmann constant, T is the absolute temperature and V is the sample volume. As a whole, the scattered intensity is then proportional to the osmotic compressibility as:

$$I_s = Ac \left(\frac{\partial n}{\partial c}\right)^2 k_B T \left(\frac{\partial \pi}{\partial c}\right)^{-1}, \tag{3}$$

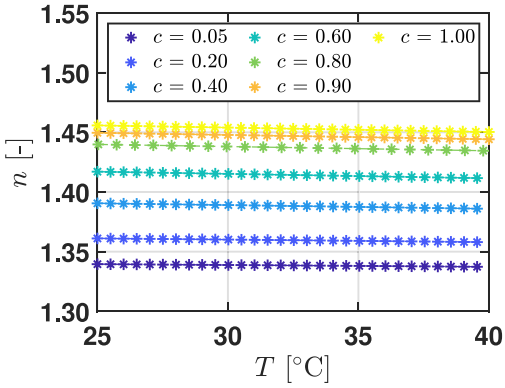

(a) Refractive index vs. Temperature for different concentrations.

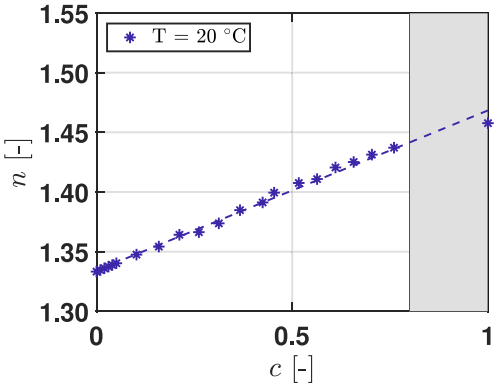

(b) Refractive index vs. Concentration at $T = 20$ °C.

Fig. 3. Refractive index characterization.

where A is an instrumental constant. The refractive index increment $\partial n/\partial c$ of the solution with respect to the solvent can be evaluated independently from n measurements of the solution at different polymer concentration. Thus, from the measured scattered intensity I_s, the osmotic compressibility is retrieved exploiting Eq. (3). Eventually, since the measurements of I_s are performed as a function of the polymer concentration c, from the numerical integration of $\chi_c(c)$, we get the osmotic pressure.

The measurements are performed with a custom-made light scattering setup, equipped with a 70 mW doubled Nd-YAG laser (wavelength $\lambda = 532$ nm), a photomultiplier mounted on a rotating arm and a temperature-controlled sample holder, which allows for careful filtration of the samples with 0.2 μm nylon membrane syringe filters (Pall®, Port Washington (NY), United States), without opening the cuvette lid. All measurements are made at a scattering angle of $\theta = 90°$, corresponding to $q \simeq 22$ μm^{-1} and the relative uncertainty on the intensity is at most $\Delta I/I \simeq 5\%$. In this case, the maximum analyzed concentration is $c = 0.8$. Absolute calibration of the scattering signal to get the instrumental constant A is made with a reference aqueous micellar solution of Triton X-100, a non-ionic surfactant, which forms micelles in water of molar mass $M_w \simeq 90$ kDa [19]; in particular, the reference signal is taken from a $c = 0.01$ Triton solution at $T = 20$ °C.

2.2.4. Density

Density measurements are made in the thermal bath with a Poulten Selfe & Lee® 541/09 hydrometer (Burnham-on-Crouch, United Kingdom), which is calibrated at $\bar{T} = 20$ °C in the density range 1000–1050 kg/m^3. For measures at temperatures higher than $\bar{T}$, we recalibrated the hydrometer by measuring the density of a test water-glycerol solution, which is well characterized in terms of its density temperature dependence [20].

2.2.5. Dynamic viscosity

Viscosity measurements are performed with two calibrated Ubbelohde microviscometers (Xylem Analytics GmbH®, Weilheim, Germany, filling volume 3 ml, measurement ranges 0.4–6 and 1.2–18 mm^2/s, respectively), immersed in the Haake F3 thermostat. The dynamic viscosity at a given temperature $\mu = \rho\nu$ is then obtained from the measured kinematic viscosity ν and density ρ. For each temperature and polymer concentration, the measurement has been repeated three times.

For samples with a kinematic viscosity higher than 18 mm^2/s, we resorted on a different method, already tested for polymer solutions [21]. We measured the settling speed of a steel ball G100 (radius $b = 250$ μm, density $\rho_B \simeq 8$ g/cm^3), which is related to the fluid dynamic viscosity by the Stokes' velocity $v_s = 2(\rho_B - \rho)gb^2/(9\mu)$. A glass cuvette (square cross section 1 × 1 cm^2, height 4 cm) was partially filled with the solution and put in the water thermostat, and for each temperature the probe ball was gently inserted in the solution with the help of an Eppendorf micropipette tip partially immersed in the fluid, such that the fall is $h = 3$ cm. The settling speed $v_s = h/\Delta t$ was evaluated by filming the settling bead from h in a time Δt with an accuracy of the order of 10 ms.

2.2.6. Thermal properties

The thermophysical quantities of the PAGB2000 aqueous solutions, namely thermal conductivity (k), thermal diffusivity (α) and isobaric specific heat capacity (c_p), are evaluated with the Thermal Lens (TL) technique, an all-optical, fast and non-invasive method, which enables assessing the opto-thermal properties of simple and complex fluids from the temporal variation of a probing laser beam intensity that is weakly absorbed by the analyzed sample [22,23].

The TL effect is based on the partial absorption of the laser beam light: by heating up the sample locally, the consequent thermal expansion turns into a local refractive index inhomogeneity, which makes the heated region act as a lens element. In particular, neglecting the heat flow along the optical axis, the heat equation leads to a parabolic temperature profile and therefore to a negative radial refractive index distribution acting as a thin diverging lens for the propagating laser beam [24–26]. Let us consider a sample with refractive index n, absorption coefficient b and thickness l in which it is focused a Gaussian laser beam of optical power P, wavelength λ, beam waist (minimal beam size) ω_0 and Rayleigh length (distance from the waist where $\omega = \sqrt{2}\omega_0$) $z_R = \pi{\omega_0}^2/\lambda$. Taking into account also aberrations and assuming that the sample is positioned at a distance $z = \sqrt{3}z_R$ from the beam waist, the time-dependent central beam intensity variation, i.e. the TL signal, can be written as $I(t) = I(0)/(1 + f(t) + \frac{1}{2}f(t)^2)$, where

$$f(t) = \frac{\pi}{6}\frac{\vartheta_{th}}{1 + \tau_{th}/t}, \tag{4}$$

with the dimensionless *thermal lens number* ϑ_{th} and the characteristic heat diffusion time τ_{th} over the beam spot size ω defined as follows

$$\vartheta_{th} = -\frac{Pbl}{k\lambda}\frac{\partial n}{\partial T} \quad \text{and} \quad \tau_{th} = \frac{{\omega_0}^2}{\alpha}. \tag{5}$$

Therefore, the sample thermal conductivity and diffusivity can be simultaneously extracted by fitting the measured TL signal, to get ϑ_{th} and τ_{th} [27]. Once k and α are known, the isobaric specific heat capacity is immediately retrieved since $c_p = k/(\rho\alpha)$. It is worth noting that in binary mixtures and colloidal suspensions, thermo-diffusive phenomena arising from the optically-generated thermal gradient cause an additional lens effect [28,29]. However, it can be unambiguously traced out since it sets up on time-scales that are related to the Brownian mass diffusivity D and therefore are much larger than τ_{th}. The TL technique has been recently used also to measure the thermal expansivity in thermosensitive polymer solutions [30].

Our custom-made experimental setup is equipped with a near-infrared laser source at $\lambda = 976$ nm, which exploits a weak vibrational band of water with absorption coefficient $b_S \simeq 0.55$ cm^{-1} at $T = 20$ °C. The laser is focused by a lens of focal length $f = 50$ mm to a beam spot size $\omega_0 \simeq 30$ μm in a cylindrical quartz sample cell (Hellma 165QS, Müllheim, Germany), of thickness $l = 1$ mm and internal diameter 9 mm, which has an external jacket for water circulation coming from an external water bath (Lauda Loop L100, Lauda-Königshofen, Germany, sensitivity 0.1 °C) in order to carefully control the sample temperature. The cell is mounted on a micrometric translator, allowing for the optimal positioning along the optical axis for the maximization of the TL effect (at $z = \sqrt{3}z_R$) and is filled through capillary PTFE tubing connected to the cell stoppers. The signal is eventually detected by a fast pinhole photodiode, acquired and elaborated by a custom-made software. Further details on the TL apparatus can be found in [31]. The samples thermal properties have been measured up to a concentration of $c = 0.8$ and the measurements are repeated four times for each temperature, showing relative uncertainties on the fitting parameters not exceeding 3%.

For the evaluation of k from the thermal lens number ϑ_{th}, the refractive index temperature derivatives are extracted from the T-dependent measurements of n performed with the refractometer. Moreover, we considered also the small absorption of the PAGB2000 detected at the probing wavelength and the full-temperature dependence of the water absorption coefficient $b_S(T)$ [32]. In particular, for the pure polymer we measured with a UV–Vis-NIR spectrophotometer (JASCO Corp. V-570, Tokyo, Japan), an absorption coefficient $b_P \simeq 0.05$ cm^{-1} at $\lambda = 976$ nm and $T \simeq 25$ °C. Thus, for a given temperature and concentration, the sample absorption coefficient is evaluated as $b(\phi, T) = b_P\phi + b_S(T)(1 - \phi)$, where $\phi = c\rho/\rho_P$ is assumed to be the polymer volume fraction at a given mass concentration c, solution density ρ and polymer density ρ_P.

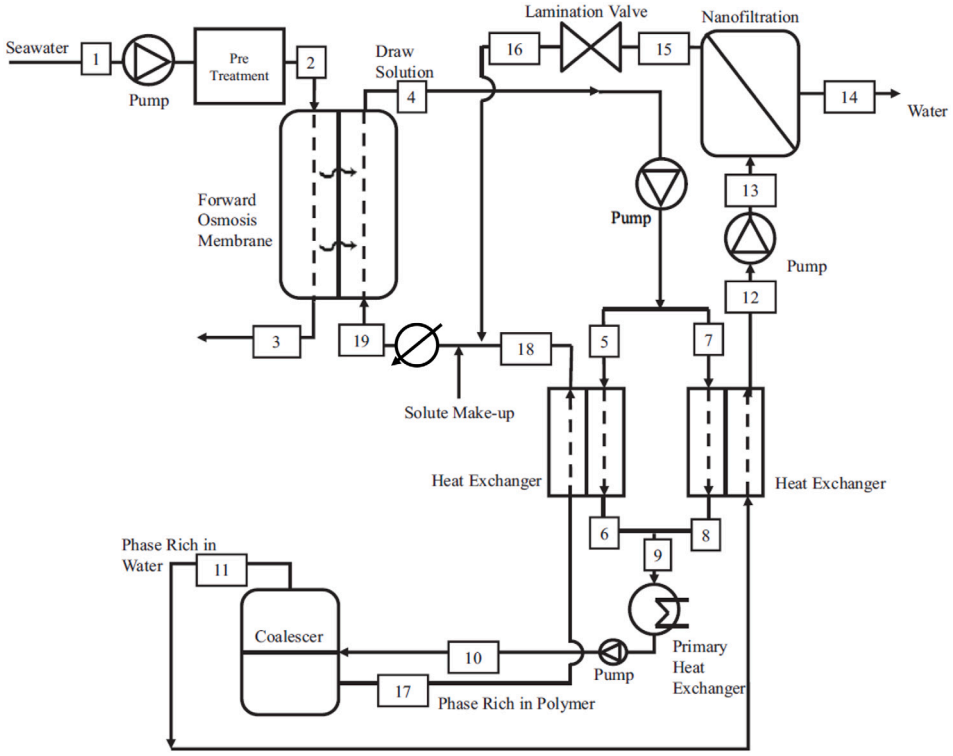

Fig. 4. Scheme of the forward osmosis plant modeled with the tested thermoresponsive copolymer as draw solute.

2.2.7. Desalination plant

The measured properties are used in a computational model [14] to simulate a desalination process via Forward Osmosis. The scheme of the plant is reported in Fig. 4 to help the reader.

The seawater enters the plant (pt. 1), and after a pre-treatment goes in the FO membrane (pt. 2). Within the membrane the seawater stream is split in two: a highly salt-concentrated stream, that leaves the membrane (pt. 3), and a fresh water stream. The latter dilutes the concentrated polymeric draw solution, which enters the membrane (pt. 19). Eventually, the diluted draw solution leaves the membrane (pt. 4) and undergoes a regeneration process in which fresh water and polymeric solutions are separated.

The membrane module configuration is counter-current to maximize the permeation driving force. The membrane is oriented in the so called "FO mode", in which the dense active layer is faced against the feed solution [33]. A regeneration temperature of 76 °C was selected, which is significantly higher than the LCST, as the higher velocity of the phase separation significantly overcomes the thermodynamic drawbacks of using higher temperature heat source. The thermodynamic conditions of the most relevant points in the FO process are reported in Appendix.

To evaluate the performances of the plant three parameters are used:

- Recovery Ratio (RR) [-]: the ratio between the freshwater flowrate extracted from the seawater (V_w) and the seawater flowrate that enters the membrane (V_{in}):

$$RR = \frac{V_w}{V_{in}}. \tag{6}$$

- Specific Electric Consumption (E_{el}) [kWh/m^3]: the ratio between the electricity consumed and the freshwater produced:

$$E_{el} = \frac{E_{el,tot}}{V_w}. \tag{7}$$

- Specific Heat Consumption (Q_{th}) [kWh/m^3]: the ratio between the requested heat and the freshwater produced:

$$Q_{th} = \frac{Q_{th,tot}}{V_w}. \tag{8}$$

3. Experimental results

The results of the physical–chemical properties characterization are here reported in term of:

- refractive index, phase behavior diagram, osmotic pressure;
- density, dynamic viscosity;
- thermal conductivity, thermal diffusivity, isobaric specific heat capacity.

The modeling performance is checked, with respect to the experimental values, in term of MRD and $MARD$ defined as follows (where z_i is a generic quantity):

$$MRD = \frac{1}{N}\sum_{i=1}^{N}\frac{z_{i,meas} - z_{i,mod}}{z_{i,meas}}\ (i) \text{ and } MARD = \frac{1}{N}\sum_{i=1}^{N}\frac{|z_{i,meas} - z_{i,mod}|}{z_{i,meas}}\ (ii). \tag{9}$$

3.1. Refractive index

The characterization of this property is fundamental, as reported in Section 2, to compute all the related properties. Refractive Index is reported as a function of temperature (Fig. 3(a)) and concentration (Fig. 3(b)).

The results show that n strongly depends on the concentration, showing a monotonic increase. On the other hand the dependence on temperature is mild, reporting a slightly-monotonic decrease.

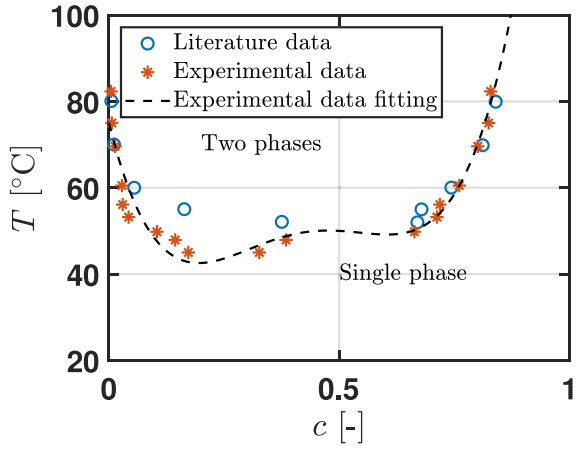

Fig. 5. Phase diagram of PAGB2000: literature data [16] (dots), experimentally determined values (stars), and experimental data fitting (dashed line).

3.2. Phase diagram

As stated in Section 2.2.2 the phase behavior diagram is obtained comparing the refractive indexes of the diluted and concentrated phases with the solution one, reported in Fig. 3(b), at $T = 20$ °C.

The phase diagram is reported in Fig. 5 and it is compared with the one measured by Inada et al. [16]. Despite the overall similarity, our result shows a minimum of the phase-separation curve around $c = 0.2$ that was not individuated in the previous investigation likely due to the different starting concentration of $c = 0.5$ from which the phase behavior was extracted, making the detection of separation at lower dilutions unfeasible. It is worth noticing that the peculiar shape of the curve may be related to the polydispersity of the polymer chains that can affect the position of the minimum of the coexistence curve, which does not necessarily coincide with the LCST [34].

According to the phase diagram, suitable separation temperatures to obtain a water-rich solution with a very small amount of polymer are in the range of 70–90 °C.

The experimental data are fitted as:

$$T(c) = 1909.1c^4 - 3245.3c^3 + 1902.1c^2 - 428.6c + 75.1. \quad (10)$$

3.3. Osmotic pressure

The experimental campaign has been conducted to evaluate the osmotic pressure at four different temperatures and the results are reported in Fig. 6. Each experimental data series is fitted with a power-law function:

$$\pi(c) = a_i c^{b_i}, \quad (11)$$

where a_i and b_i depend on the temperature. Both parameters show a linear dependence on the temperature (Fig. 7(a) and (b)).

Therefore:

$$\pi(c,T) = (118.37 - 1.48T)c^{(0.02T+1.32)}. \quad (12)$$

The model predicts well the experimental results with a $MRD = 0.57\%$ and $MARD = 9.67\%$. Moreover, the obtained data agree with the ones reported in [16], in which the osmotic pressure value was measured only at 25 °C.

Worth of mentioning is that at the high concentrations tested ($c > 0.5$) the Van't Hoff equation, used for diluted solutions and commonly adopted to describe the osmotic pressure behavior, cannot be used as it tends to overestimate the osmotic pressure values (cf. black dashed lines in Fig. 6(a) and (b)).

Moreover, a lower osmotic pressure than that of the ideal mixture is expected when attraction between polymer chains occurs, which will then lead to phase separation at higher temperatures.

3.4. Density

From the experimental campaign the solution density, for each concentration, shows a linear decrease with temperature (Fig. 8(a)). As the dependence of the density on the concentration cannot be easily determined using the same plot, the experimental data are elaborated and plotted against concentration at fixed temperatures (Fig. 8(b)). The analysis shows a quadratic dependence of the density with respect to concentration:

$$\rho(c) = C_{1,i}c^2 + C_{2,i}c + C_{3,i}. \quad (13)$$

A linear dependence on the temperature is obtained (Fig. 9) for all the three parameters (i.e., C_1, C_2 and C_3).

Therefore:

$$\rho(c,T) = (1.83T - 190.85)c^2 + (-2.40T + 252.39)c + (-0.06T + 993.76). \quad (14)$$

The model predicts very well the experimental results with a $MRD = -0.02\%$ and $MARD = 0.04\%$.

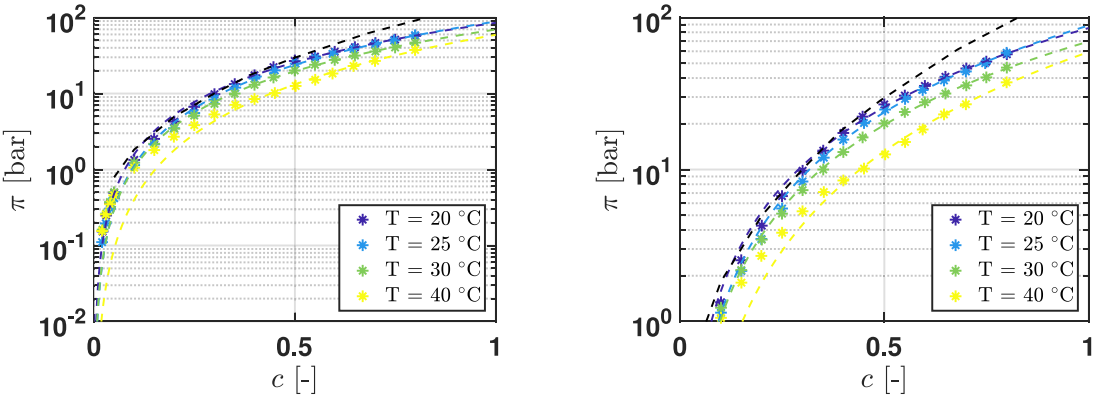

(a) Full range. (b) Zoom on *y-axis*.

Fig. 6. Osmotic pressure vs. Concentration for different temperatures, experimental results (stars) and model (dashed line), valid for $c > 10\%$. The black dashed line is the Van't Hoff equation.

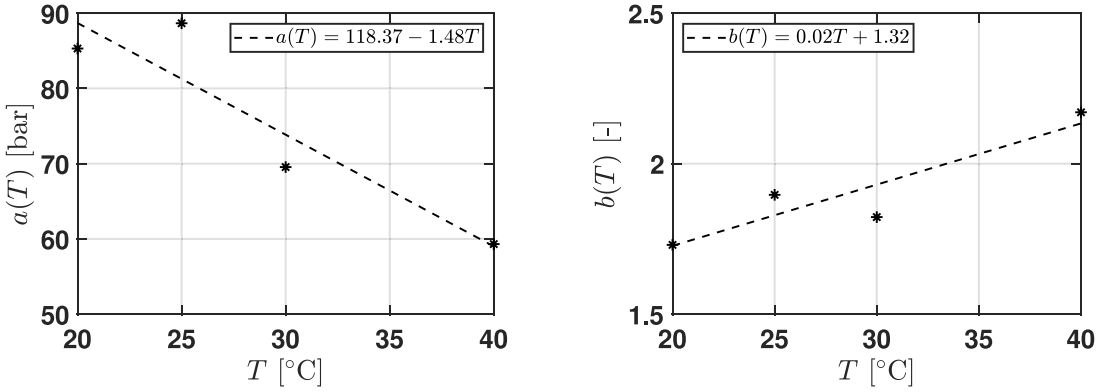

(a) $a(T)$ vs. Temperature. (b) $b(T)$ vs. Temperature.

Fig. 7. Osmotic pressure fitting parameters dependence on temperature (Eq. (11)).

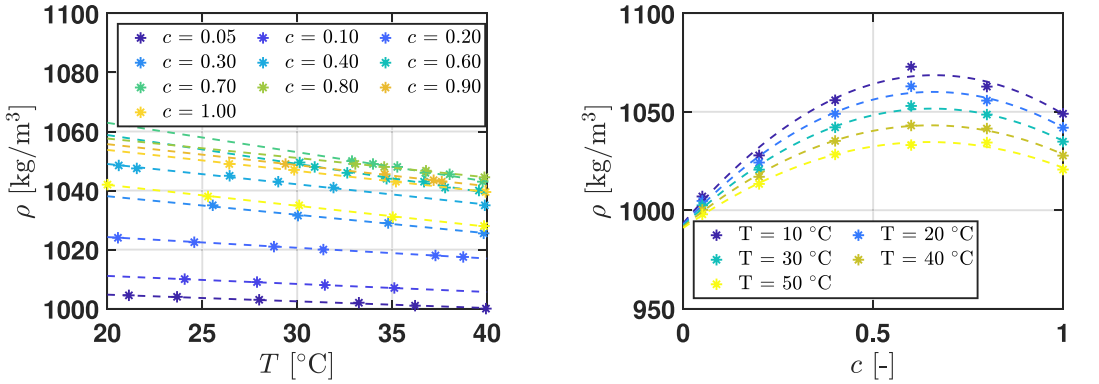

(a) Density vs. Temperature for different concentrations. (b) Density vs. Concentration at different temperatures.

Fig. 8. Density characterization, experimental results (stars) and model (dashed line).

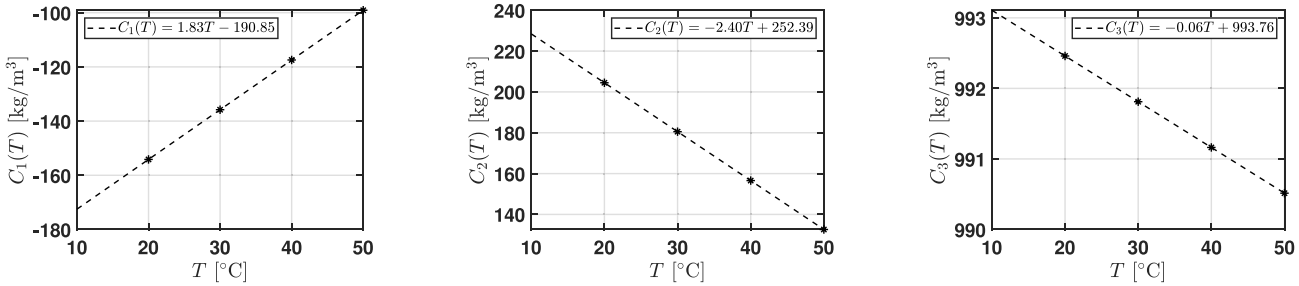

(a) $C_1(T)$ vs. Temperature. (b) $C_2(T)$ vs. Temperature. (c) $C_3(T)$ vs. Temperature.

Fig. 9. Density fitting parameters dependence on temperature (Eq. (13)).

3.5. Dynamic viscosity

The viscosity of the solution, for each concentration, is plotted against $(T^{-1} - T_0^{-1})$ [K] (Fig. 10) in accordance with the Arrhenius law:

$$\mu = \mu_{0,i} \exp\left\{ \left(\frac{\Delta H}{R}\right)_i \left(\frac{1}{T} - \frac{1}{T_0}\right) \right\}, \tag{15}$$

where T_0 is the reference temperature set as 298.15 K, $\mu_{0,i}$ is the viscosity value at the reference temperature, ΔH_i is the activation energy in Jmol^{-1}, R is the universal gas constant set as 8.314 Jmol^{-1}K^{-1}, and the subscript i refers to each of the concentrations tested.

Hence, the results are fitted with an exponential function, i.e., $y = a\exp(bx)$, where a represents $\mu_{0,i}$ and b represents $(\Delta H/R)_i$, respectively. The obtained coefficients are plotted as a function of concentration (Fig. 11(a) and (b)).

$(\Delta H/R)_i$ depends linearly on concentration, whereas $\mu_{0,i}$ shows a power law function with respect to concentration:

$$\mu_{0,i} = \mu_0 \left\{ \frac{c}{c_0} \right\}^m, \tag{16}$$

for $c \geq 0.2$, μ_0 is the viscosity at the reference concentration, i.e., $c_0 = 0.05$ and m is the power law exponent, equal to 2.912.

Therefore, the dependence of viscosity on both temperature and concentration (Eq. (15)) can be made explicit:

$$\mu(c,T) = 0.09 \exp\left\{ (3321.5c + 2160.1)\left(\frac{1}{T} - \frac{1}{298.15}\right) \right\} \left\{ \frac{c}{0.053} \right\}^{2.912}. \tag{17}$$

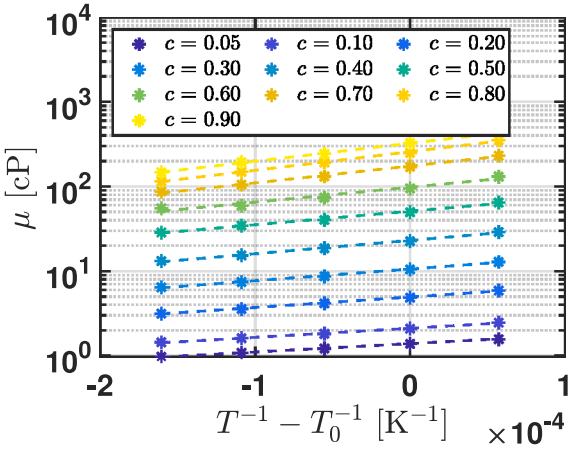

Fig. 10. Dynamic viscosity vs. Temperature for different concentrations, experimental results (stars) and model (dashed line).

In Fig. 12 both the experimental results and the model are reported. ($MRD = -17\%$ and $MARD = 20\%$).

On the other hand, the fitting performance is improved using a purely empirical correlation for $\mu_{0,i}$, as follows:

$$\mu_{0,i} = 544c^{3.55} + 2.11\left(\frac{c}{0.2}\right) + 0.89, \tag{18}$$

where $\mu_{water}(T_0) = 0.89$ cP. This model better predicts both the linear behavior, at low concentrations ($c < 0.2$), and the exponential one, at high concentrations ($c \geq 0.2$). Additionally, both MRD and $MARD$ are reduced up to −2% and 6%, respectively.

3.6. Thermal properties

Eventually, the thermal properties are characterized, as reported in Section 2.2.6, through Eqs. (4) and (5) to determine the thermal conductivity and diffusivity, respectively. Hence, the isobaric specific heat capacity is retrieved from:

$$c_p = \frac{k}{\rho\alpha}. \tag{19}$$

In the open literature, to the authors knowledge, very few information can be found regarding thermal properties and concentration for polymeric solutions, hence this work represents a first step towards a more complete characterization of highly concentrated polymeric solutions.

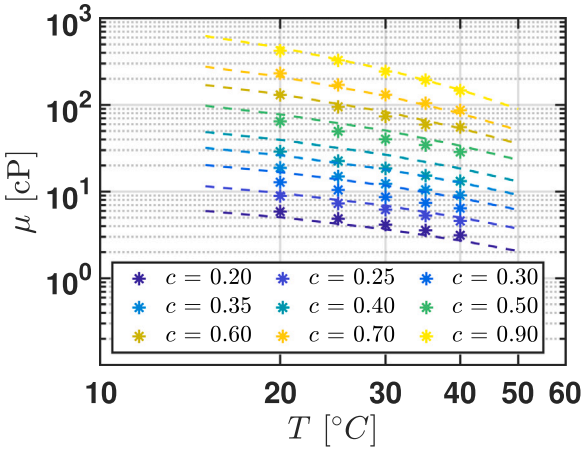

Fig. 12. Dynamic viscosity vs. Temperature for different concentrations, experimental results (stars) and model (dashed line).

3.6.1. Thermal conductivity

The obtained results show a negligible dependence of the thermal conductivity on temperature within the investigated temperature range (i.e., 24 - 40 °C), being the difference in thermal conductivity always lower than the measurement uncertainty. On the other hand, the thermal conductivity strongly depends on the concentration, specifically, it decreases as the polymer concentration increases, indicating the insulating nature of the chosen polymer [35] (see Fig. 13).

A quadratic dependence on concentration is found:

$$k(c) = 0.591c^2 - 1.060c + 0.617. \tag{20}$$

3.6.2. Thermal diffusivity

Regarding the thermal diffusivity, a similar behavior as the thermal conductivity is found (see Fig. 14).

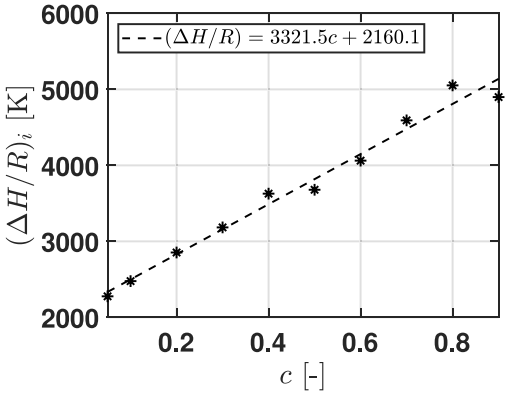

(a) $\Delta H/R$ vs. Concentration.

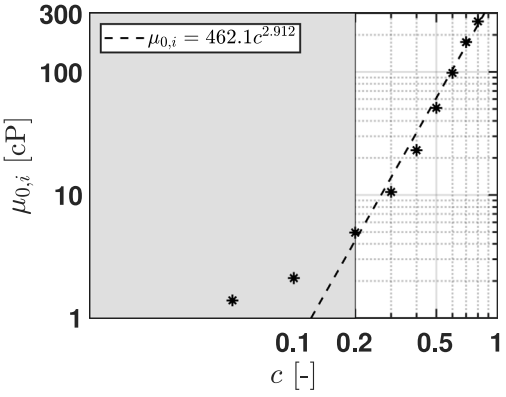

(b) $\mu_{0,i}$ vs. Concentration.

Fig. 11. Parameters fit for extrapolating viscosity dependence on concentration (Eq. (15)).

Table 1
Comparison of performance results with other technologies [36] and [37].

Variable	Unit of measurement	MSF	MED	RO	ED	FO_{old}	FO_{new}
RR	[%]	0.6 - 6	6 - 38	10 - 51	25 - 50	11 - 19	8 - 13
E_{el}	[kWh/m^3]	2.5 - 5	2 - 2.5	4 - 6	2.6 - 5.5	0.7 - 0.9	0.6 - 1
Q_{th}	[kWh/m^3]	53 - 65	40 - 64	none	none	50 - 81	40 - 80

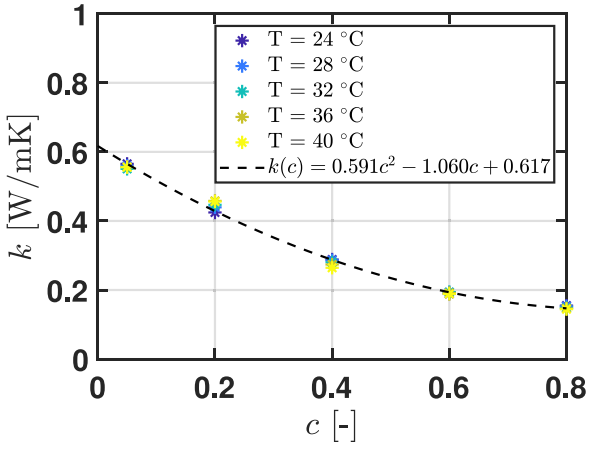

Fig. 13. Thermal conductivity vs. Concentration at different temperatures.

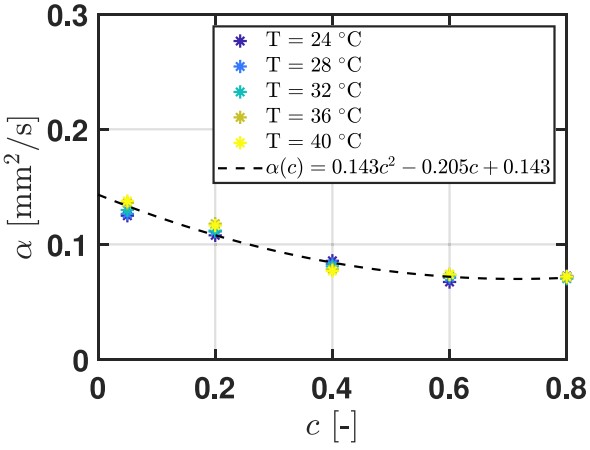

Fig. 14. Thermal diffusivity vs. Concentration at different temperatures.

A quadratic dependence on concentration is found:

$$\alpha(c) = 0.143c^2 - 0.205c + 0.143. \quad (21)$$

3.6.3. Isobaric specific heat capacity

Once defined ρ, k and α, using Eq. (19), it is found how the specific heat capacity varies with respect to the concentration (see Fig. 15).

Specifically, a linear dependence on concentration is found:

$$c_p(c) = 4438.2 - 3072.4c. \quad (22)$$

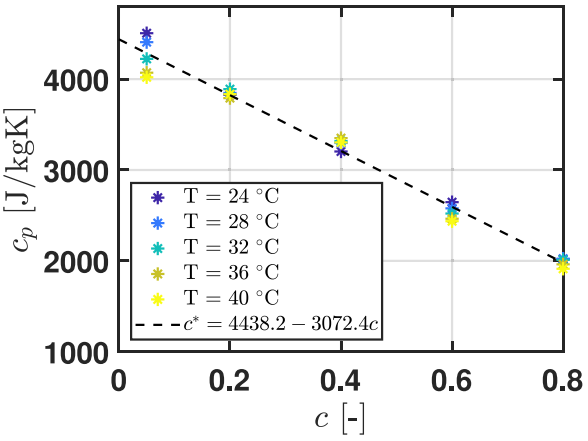

Fig. 15. Specific heat capacity vs. Concentration at different temperatures.

4. Discussion

The properties, once experimentally determined, are inserted in the model and the same analysis reported in [14] has been performed. The results are here compared in terms of: recovery ratio, specific electric consumption and specific heat consumption.

Specifically, ten conditions are considered: two seawater flowrates (m_F = 12 and 18 kg/min), and five draw agent flowrates (m_D = 8, 10, 12, 14 and 16 kg/min).

The RR (Eq. (6)) is a key parameter to understand the quality of the desalination process through FO membranes. Being the parameter that represents the quantity of pure water that is extracted from the seawater, it is affected by the draw agent osmotic pressure, which decreases as the temperature increases (cf. Fig. 6). Hence, considering the osmotic pressure dependence on both temperature and concentration, there is a reduction of about 30% (Fig. 16).

Along with a reduction in the RR, we envisage an increase in the specific electric consumption (Eq. (7)) of about 40% (Fig. 17(a)). This result is consistent with the definition reported in Eq. (7) being the numerator equal for the two modeled cases, whereas the denominator decreases as previously noticed.

On the other hand, a reduction of about 20% in the thermal energy (Eq. (8)) required to warm the solution from T_9 (T_{mix}) to T_{10} (T_{reg}) (Fig. 4) is envisaged (Fig. 17(b)). This is mainly caused by the reduction in the draw solution flowrate (m_D), which decreases as the water flowrate that crosses the membrane is less.

In Table 1, the key performance parameters of both models (i.e., old and new) and of other desalination technologies, already studied and analyzed in the open literature [36,37], are reported.

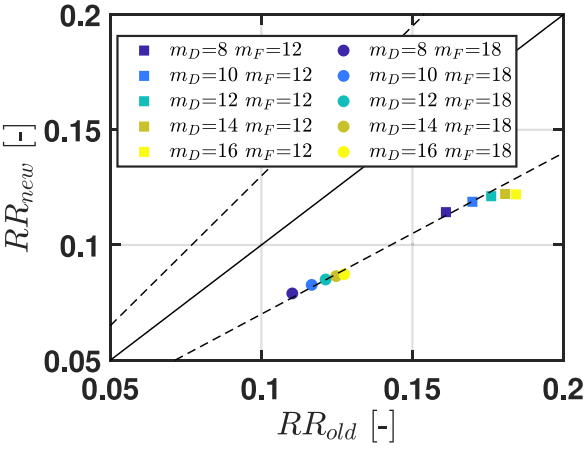

Fig. 16. Parity plot representing the the variation of the Recovery Ratio between the old and new model (boundaries ±30%).

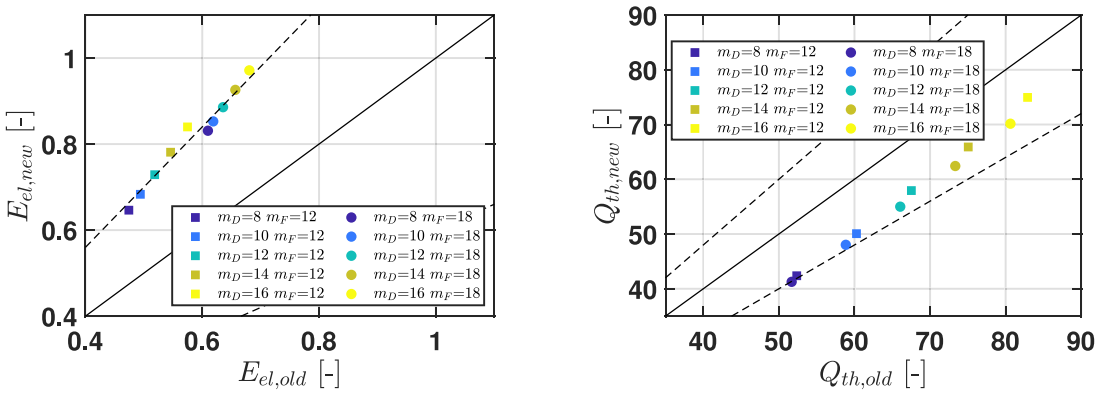

(a) Specific Electric Consumption (boundaries ±40%).

(b) Specific Heat Consumption (boundaries ±20%.)

Fig. 17. Parity plots representing the variation between the old and new model.

The differences between the outputs of the two FO models show that the performances obtained with the updated properties are slightly worse, in particular with respect to the drinkable water production (RR).

On the other hand, comparing the FO performances with the ones of other technologies, we can state that FO is still very competitive thanks to the very limited electric consumption.

However, being the RR considerably lower with respect to more affirmed technologies (i.e., RO and ED) [36,37], efforts have to be made to fill this gap, perhaps acting on the membrane surface area available to perform the process.

5. Conclusions

In this study, we focused on characterizing the draw agent polymeric solution, particularly examining PAGB2000 as a potential draw agent for forward osmosis (FO) in water desalination. Our analysis of the experimental results yielded the following conclusions:

- The osmotic pressure exhibited a linear dependence on temperature and a power-law dependence on concentration.
- The density of the polymeric mixture displayed a linear relationship with temperature and a quadratic relationship with concentration, reaching a maximum at approximately $c \approx 0.6$.
- The viscosity of the polymeric mixture could be accurately described by the Arrhenius law, providing reliable estimations for concentrations exceeding 0.2.
- Thermal conductivity and thermal diffusivity both exhibited quadratic dependencies on concentration, with no discernible temperature dependence within the range of temperatures investigated.

These findings played a crucial role in developing a comprehensive model for simulating the entire desalination process. Our characterization of the polymer suggests that PAGB2000 holds promise as a draw agent for FO technology. Moreover, when compared to other desalination methods, FO technology employing PAGB2000 demonstrated significant advantages in terms of energy consumption, particularly with regard to electrical consumption. However, it is important to note that FO technology does suffer from a lower recovery ratio, approximately 3 to 4 times lower than well-established technologies like reverse osmosis and electrodialysis. This aspect warrants further attention and consideration in the context of FO applications.

CRediT authorship contribution statement

Igor Matteo Carraretto: Formal analysis, Investigation, Writing – original draft. **Vincenzo Ruzzi:** Formal analysis, Investigation, Writing – original draft. **Filippo Lodigiani:** Formal analysis, Investigation. **Rosemary Colciaghi:** Investigation, Software. **Riccardo Simonetti:** Software. **Stefano Buzzaccaro:** Formal analysis, Resources, Writing – review & editing, Supervision. **Luca Molinaroli:** Conceptualization, Resources, Supervision. **Luigi Pietro Maria Colombo:** Resources, Writing – review & editing, Supervision. **Roberto Piazza:** Methodology, Resources, Writing – review & editing, Supervision. **Giampaolo Manzolini:** Conceptualization, Methodology, Resources, Writing – review & editing, Supervision, Project administration, Funding acquisition.

Declaration of competing interest

The authors declare that they have no known competing financial interests or personal relationships that could have appeared to influence the work reported in this paper.

Data availability

Data will be made available on request.

Acknowledgments

This project has received funding from the European Union's Horizon 2020 research and innovation programme under grant agreement No. 101022686 (DESOLINATION). We would like to thank both Prof. Gareth McKinley and Dr. Crystal Owens for the for helpful discussion on the polymer viscosity. Dr. Andrea Lucotti is acknowledged for his kind help with the spectrophotometer.

Appendix. Simulation results

In Table A.2 the thermodynamic conditions of the most relevant points in the FO process are reported.

Table A.2
Solute mass concentration, temperature and mass flow rates using PAGB2000 assuming an initial concentration of 0.75, and seawater and draw solution flowrates of 0.20 and 0.27 kg/s (12 and 16 kg/min), respectively. Numbers refer to Fig. 4.

Pt	c [-]	T [°C]	m [kg/s]	Note
1	0.038	20.4	0.20	Seawater intake (salt concentration)
2	0.038	20.4	0.20	Seawater after pre-treatment (salt concentration)
3	0.044	27.4	0.18	Seawater outlet (salt concentration)
4	0.68	20.4	0.29	Diluted draw solution
5	0.68	20.4	0.21	Dil. draw s. (inlet of pre-heating HEX, polymer-rich side)
6	0.68	68.0	0.21	Dil. draw s. (outlet of pre-heating HEX, polymer-rich side)
7	0.68	20.4	0.08	Dil. draw s. (inlet of pre-heating HEX, water-rich side)
8	0.68	61.0	0.08	Dil. draw s. (outlet of pre-heating HEX, water-rich side)
9	0.68	65.8	0.29	Mixed diluted draw solutions at the outlet of the HEXs
10	0.68	76.0	0.29	Diluted draw solution, inlet of coalescer
11	0.01	76.0	0.04	Water-rich phase, outlet of coalescer
12	0.01	25.7	0.04	Water-rich phase, outlet of pre-heating HEX
13	0.01	25.7	0.04	Water-rich phase, outlet of NF pump
14	0.00	25.7	0.02	Final product
15	0.02	25.7	0.02	Rejected flux from NF
16	0.02	25.7	0.02	Rejected flux from NF, after lamination valve
17	0.80	76.0	0.25	Polymer-rich phase, outlet of coalescer
18	0.80	31.5	0.25	Polymer-rich phase, outlet of pre-heating HEX
19	0.75	31.5	0.27	Concentrated draw solution

References

[1] E.J. Okampo, N. Nwulu, Optimisation of renewable energy powered reverse osmosis desalination systems: A state-of-the-art review, Renew. Sustain. Energy Rev. 140 (2021) 110712, http://dx.doi.org/10.1016/j.rser.2021.110712.

[2] C. Skuse, A. Gallego-Schmid, A. Azapagic, P. Gorgojo, Can emerging membrane-based desalination technologies replace reverse osmosis? Desalination 500 (2021) 114844, http://dx.doi.org/10.1016/j.desal.2020.114844.

[3] M. Shatat, M. Worall, S. Riffat, Opportunities for solar water desalination worldwide, Sustain. Cities Soc. 9 (2013) 67–80, http://dx.doi.org/10.1016/j.scs.2013.03.004.

[4] A. Al-Karaghouli, L.L. Kazmerski, Energy consumption and water production cost of conventional and renewable-energy-powered desalination processes, Renew. Sustain. Energy Rev. 24 (2013) 343–356, http://dx.doi.org/10.1016/j.rser.2012.12.064.

[5] P. Gabrielli, M. Gazzani, N. Novati, L. Sutter, R. Simonetti, L. Molinaroli, G. Manzolini, M. Mazzotti, Combined water desalination and electricity generation through a humidification-dehumidification process integrated with photovoltaic-thermal modules: Design, performance analysis and techno-economic assessment, Energy Convers. Manag. X 1 (2019) 100004, http://dx.doi.org/10.1016/j.ecmx.2019.100004.

[6] M. Qasim, N.A. Darwish, S. Sarp, N. Hilal, Water desalination by forward (direct) osmosis phenomenon: A comprehensive review, Desalination 374 (2015) 47–69, http://dx.doi.org/10.1016/j.desal.2015.07.016.

[7] M. Amjad, J. Gardy, A. Hassanpour, D. Wen, Novel draw solution for forward osmosis based solar desalination, Appl. Energy 230 (2018) 220–231, http://dx.doi.org/10.1016/j.apenergy.2018.08.021.

[8] Q. Long, Y. Jia, J. Li, J. Yang, F. Liu, J. Zheng, B. Yu, Recent advance on draw solutes development in forward osmosis, Processes 6 (9) (2018) 165, http://dx.doi.org/10.3390/pr6090165.

[9] J.R. McCutcheon, R.L. McGinnis, M. Elimelech, Desalination by ammonia–carbon dioxide forward osmosis: influence of draw and feed solution concentrations on process performance, J. Membr. Sci. 278 (1–2) (2006) 114–123, http://dx.doi.org/10.1016/j.memsci.2005.10.048.

[10] J.-j. Kim, H. Kang, Y.-S. Choi, Y.A. Yu, J.-C. Lee, Thermo-responsive oligomeric poly (tetrabutylphosphonium styrenesulfonate) s as draw solutes for forward osmosis (FO) applications, Desalination 381 (2016) 84–94, http://dx.doi.org/10.1016/j.desal.2015.11.013.

[11] Y. Zhong, X. Feng, W. Chen, X. Wang, K.-W. Huang, Y. Gnanou, Z. Lai, Using UCST ionic liquid as a draw solute in forward osmosis to treat high-salinity water, Environ. Sci. Technol. 50 (2) (2016) 1039–1045, http://dx.doi.org/10.1021/acs.est.5b03747.

[12] Y. Cai, R. Wang, W.B. Krantz, A.G. Fane, et al., Exploration of using thermally responsive polyionic liquid hydrogels as draw agents in forward osmosis, RSC Adv. 5 (118) (2015) 97143–97150, http://dx.doi.org/10.1039/C5RA19018E.

[13] G. Gwak, B. Jung, S. Han, S. Hong, Evaluation of poly (aspartic acid sodium salt) as a draw solute for forward osmosis, Water Res. 80 (2015) 294–305, http://dx.doi.org/10.1016/j.watres.2015.04.041.

[14] R. Colciaghi, R. Simonetti, L. Molinaroli, M. Binotti, G. Manzolini, Potentialities of thermal responsive polymer in forward osmosis (FO) process for water desalination, Desalination 519 (2021) 115311.

[15] A. Inada, K. Yumiya, T. Takahashi, K. Kumagai, Y. Hashizume, H. Matsuyama, Development of thermoresponsive star oligomers with a glycerol backbone as the draw solute in forward osmosis process, J. Membr. Sci. 574 (2019) 147–153, http://dx.doi.org/10.1016/j.desal.2021.115311.

[16] A. Inada, K. Kumagai, H. Matsuyama, Effect of the molecular weights of thermoresponsive polyalkylene glycol draw solutes on forward osmosis performance, Sep. Purif. Technol. 252 (2020) 117462, http://dx.doi.org/10.1016/j.seppur.2020.117462.

[17] H.L. Swinney, Critical phenomena in fluids, in: Photon Correlation and Light Beating Spectroscopy, Springer, 1974, pp. 331–383, http://dx.doi.org/10.1007/978-1-4615-8906-8_9.

[18] L.D. Landau, E.M. Lifshitz, Statistical Physics, Vol. 5, Elsevier, 2013.

[19] R. Piazza, M. Campello, S. Buzzaccaro, F. Sciortino, Phase behavior and microscopic dynamics of a thermosensitive gel-forming polymer, Macromolecules 54 (8) (2021) 3897–3906, http://dx.doi.org/10.1021/acs.macromol.0c02785.

[20] D.R. Lide, CRC Handbook of Chemistry and Physics, Vol. 85, CRC Press, 2004.

[21] S. Buzzaccaro, V. Ruzzi, T. Faleo, R. Piazza, Microrheology of a thermosensitive gelling polymer for cell culture, J. Chem. Phys. 157 (17) (2022) 174901, http://dx.doi.org/10.1063/5.0086533.

[22] M.A. Proskurnin, D.S. Volkov, T.A. Gor'kova, S.N. Bendrysheva, A.P. Smirnova, D.A. Nedosekin, Advances in thermal lens spectrometry, J. Anal. Chem. 70 (3) (2015) 249–276, http://dx.doi.org/10.1134/S1061934815030168.

[23] M. Liu, M. Franko, Thermal lens spectrometry: Still a technique on the horizon? Int. J. Thermophys. 37 (7) (2016) http://dx.doi.org/10.1007/s10765-016-2072-y.

[24] J.P. Gordon, R.C.C. Leite, R.S. Moore, S.P.S. Porto, J.R. Whinnery, Long-transient effects in lasers with inserted liquid samples, J. Appl. Phys. 36 (1) (1965) 3–8, http://dx.doi.org/10.1063/1.1713919.

[25] J. Whinnery, D. Miller, F. Dabby, Thermal convention and spherical aberration distortion of laser beams in low-loss liquids, IEEE J. Quantum Electron. 3 (9) (1967) 382–383, http://dx.doi.org/10.1109/JQE.1967.1074612.

[26] S. Wu, N.J. Dovichi, Fresnel diffraction theory for steady-state thermal lens measurements in thin films, J. Appl. Phys. 67 (3) (1990) 1170–1182, http://dx.doi.org/10.1063/1.346057.

[27] R. Rusconi, E. Rodari, R. Piazza, Optical measurements of the thermal properties of nanofluids, Appl. Phys. Lett. 89 (26) (2006) 261916, http://dx.doi.org/10.1063/1.2425015.

[28] M. Giglio, A. Vendramini, Thermal lens effect in a binary liquid mixture: A new effect, Appl. Phys. Lett. 25 (10) (1974) 555–557, http://dx.doi.org/10.1063/1.1655308.

[29] R. Rusconi, L. Isa, R. Piazza, Thermal-lensing measurement of particle thermophoresis in aqueous dispersions, J. Opt. Soc. Amer. B 21 (3) (2004) 605–616, http://dx.doi.org/10.1364/JOSAB.21.000605.

[30] V. Ruzzi, S. Buzzaccaro, R. Piazza, Thermal lens measurements of thermal expansivity in thermosensitive polymer solutions, Polymers 15 (5) (2023) 1283, http://dx.doi.org/10.3390/polym15051283.

[31] E. Lattuada, S. Buzzaccaro, R. Piazza, Thermophoresis in self-associating systems: Probing poloxamer micellization by opto-thermal excitation, Soft Matter 15 (10) (2019) 2140–2151, http://dx.doi.org/10.1039/C8SM02386G.

[32] M. Baptista, C. Tran, Structural investigation of the effects of nonelectrolytes and surfactants on water by thermal lens spectrometry, J. Phys. Chem. 99 (1995) 12952, http://dx.doi.org/10.1021/j100034a039.

[33] J.R. McCutcheon, M. Elimelech, Influence of concentrative and dilutive internal concentration polarization on flux behavior in forward osmosis, J. Membr. Sci. 284 (1–2) (2006) 237–247, http://dx.doi.org/10.1016/j.memsci.2006.07.049.
[34] R. Koningsveld, Liquid-liquid equilibria in multicomponent polymer systems, Discuss. Faraday Soc. 49 (1970) 144–161, http://dx.doi.org/10.1039/DF9704900144.
[35] D. Van Krevelen, Properties of Polymers, Elsevier, New York, 1976.
[36] M.A. Abdelkareem, M.E.H. Assad, E.T. Sayed, B. Soudan, Recent progress in the use of renewable energy sources to power water desalination plants, Desalination 435 (2018) 97–113, http://dx.doi.org/10.1016/j.desal.2017.11.018.
[37] M.T. Ali, H.E. Fath, P.R. Armstrong, A comprehensive techno-economical review of indirect solar desalination, Renew. Sustain. Energy Rev. 15 (8) (2011) 4187–4199, http://dx.doi.org/10.1016/j.rser.2011.05.012.